An Optimized Active Power Backflow Suppression Strategy for Cascaded H-Bridge PV Grid-Connected Inverter During Inter-Phase Short-Circuit Fault

Tao Zhao, Zixiang Sun, *Student Member, IEEE*, Zhijian Feng, Mingda Wang, *Student Member, IEEE*, Mengze Wu, *Student Member, IEEE*, and Xing Zhang, *Senior Member, IEEE*

***Abstract*—Active power backflow is a unique problem of three-phase isolated cascaded H-bridge (CHB) PV inverter during asymmetric grid voltage fault, resulting in the continuous rise of H-bridge dc-bus voltages and that the inverter will be eventually shut down and off-grid due to voltage out of control. The existing methods are able to completely suppress the active power backflow during single-phase short-circuit fault and two-phase short-circuit fault, but fails in a large operating zone when interphase short-circuit fault occurs. For this issue, this article proposes a novel multiple specific harmonic voltages injection method based on the existing fundamental-frequency zero-sequence voltage compensation strategy, which calculates and injects the optimal third, fifth, seventh, and ninth harmonic voltage according to the fault type, drop depth, and the normalized power, for minimizing the amplitude of three-phase modulation voltages and then significantly shrinking active power backflow zone of three-phase isolated CHB PV inverter. Then, the area of the active power backflow zones for different control methods is quantitatively calculated and compared by adopting the polynomial fitting to show the advantages of the proposed method. Finally, experimental results are achieved by a low voltage and low power experimental prototype to verify its effectiveness and feasibility.**

***Index Terms*—Active power backflow, cascaded H-bridge (CHB), PV power generation system, specific harmonic voltages injection.**

I. Introduction

ACCORDING to 2022 international renewable energy status report, renewable power capacity additions grew 17% in 2021 to reach a new high of more than 314GW of added capacity, and a record 175GW of solar PV was added, accounting for well over half of the renewable additions [1]. Therefore, PV power generation still has a strong development momentum and a continuously rising market size. Compared with low power PV power generation systems, large-scale PV plants can not only rapidly expand the scale of renewable energy, but also deliver further reductions in cost per watt, which is more commercially attractive [2], [3], [4].

Considering that PV inverter is the bridge that transmits the solar energy to the power grid, it is the core equipment of PV power generation system [5]. Among all the topologies, the three-phase isolated cascaded H-bridge (CHB) inverters are able to realize flexible and efficient large-capacity medium-voltage direct-linked grid connection without line-frequency transformer, which has outstanding advantages in large-scale PV power plants [6]. First of all, the modular structure can use low-voltage devices to expand the system to higher voltage and power levels [7]. Second, since high-frequency transformers already provide electrical isolation, bulky line-frequency transformers will no longer be required. Third, the multilevel output voltage allows the H-bridge (HB) to operate at a lower switching frequency, improving efficiency and achieving high-quality grid current [8], [9], [10], [11], [12]. Therefore, the three-phase isolated CHB inverters are considered as one of the most suitable topology candidates for next-generation PV inverters [11], [12], [13]. Since three-phase common dc-bus isolated CHB inverter has the advantages of no intermodule and interphase power imbalance problems, it is studied in this article due to simple control [8], [12], [14].

However, different from conventional PV inverters, the topology of three-phase CHB PV inverter is relatively special, which exists inherent active power backflow problem during low voltage ride through (LVRT) and based on the premise of asymmetric grid fault [15]. Specifically, three-phase CHB topology can be regarded as composed of three independent single-phase CHB inverters, and one phase of the converter may inversely absorb active power from the ac grid affected by negative-sequence voltages, resulting in that HB dc-bus voltage continues to rise during LVRT, and the converter will eventually be shut down and off-grid due to voltage out of control. Active power backflow will cause the inverter to fail to achieve LVRT and does not meet grid-tied standards. In addition, for large-scale PV power plants, the sudden shutdown will cause large economic

Manuscript received 7 November 2022; revised 24 February 2023; accepted 3 April 2023. Date of publication 12 April 2023; date of current version 19 May 2023. This work was supported in part by the Shandong Youth Innovation Team under Grant 2022KJ150, and in part by the Youth Project of Natural Science Foundation of Shandong Province under Grant ZR2022QE057. Recommended for publication by Associate Editor D. Vinnikov. *(Corresponding author: Zixiang Sun.)*

Tao Zhao, Zixiang Sun, and Zhijian Feng are with the Qingdao University, Qingdao 266071, China (e-mail: zt_kyyx@163.com; 13914037827@163.com; fengzhijian1992@163.com).

Mingda Wang, Mengze Wu, and Xing Zhang are with the Hefei University of Technology, Hefei 230009, China (e-mail: wmd6094@mail.hfut.edu.cn; 2020110332@mail.hfut.edu.cn; honglf@ustc.edu.cn).

Color versions of one or more figures in this article are available at https://doi.org/10.1109/TPEL.2023.3266613.

Digital Object Identifier 10.1109/TPEL.2023.3266613

losses and affect frequency stability due to larger active power shortage [16].

Lots of studies about the LVRT control strategies of CHB PV inverter have been carried out. In [17], a flexible control strategy for the operation of CHB PV inverters during unbalanced voltage sags is proposed, which injects both active and reactive power to the grid with either balanced or unbalanced currents to ensure that all HB dc-bus voltages remain balanced. In [18], the performance of cascaded multilevel PV inverter is investigated under perturbing voltage condition at point of common coupling, that is, voltage sag by robust multimode control, demonstrating its LVRT capability. In [19], a zero-sequence voltage expression is derived to control the active power flow among three phases for maintaining HB dc-bus voltage under unbalanced power generation and unsymmetrical voltage sags. In [20], an inrush current limit method for CHB multilevel grid-connected converter during LVRT is proposed. Although [17], [18], [19], [20] has made many innovative achievements, laying a theoretical foundation for the LVRT control of three-phase CHB PV inverter, the unique active power backflow problem was not mentioned and studied. In [15], active power backflow mechanism of three-phase CHB PV grid-tied inverter is explained, and an active current injection strategy (ACIS) is proposed. By injecting appropriate positive-sequence active currents into power grid, this method ensures that the power generated by positive-sequence voltages are greater than the absolute value of that generated by negative-sequence voltages. However, Zhao and Chen [15] did not consider the operating scenarios with lower output power of PV array, such as overcast, rainy day, early morning and evening, where the positive-sequence active current actually output by the inverter may be far less than the demand value, so there still exist active power backflow. Aiming at this issue, a zero-sequence voltage compensation strategy (ZSVCS) for three-phase isolated CHB PV inverter during LVRT is proposed in [21], which offsets the power redistribution of negative-sequence voltages by injecting zero-sequence voltage, so the active power in three phases is only the power generated by positive-sequence voltage. Considering that ZSVCS has no specific requirements for positive-sequence active current, it is able to theoretically suppress active power backflow under lower output power conditions. However, after adding zero-sequence voltage, the amplitude of three-phase modulation voltages significantly increases, causing overmodulation of the inverter in larger operating zone, which is not studied in [21]. In [22], the variation law of three-phase modulation voltage amplitude with normalized power and voltage drop depth is revealed and the overmodulation region by adopting ZSVCS is quantitatively given. Then, different control methods to suppress active power backflow is proposed under different fault conditions. Specifically, when single-phase short-circuit fault with ground occurs, the operation range is divided two zones. If the inverter works in zone 1, ZSVCS is adopted. If the inverter works in zone 2, ACIS is used. In this way, active power backflow is able to be completely suppress. When two-phase short-circuit fault occurs, ZSVCS will be directly used to effectively suppress active power backflow due to no overmodulation zone. When interphase short-circuit fault occurs, an adaptive zero-sequence voltage compensation strategy (AZSVCS) is proposed, which is able to reduce the active power backflow zone compared with ZSVCS, but still fail to suppress it in the operating zone with lower output power and deeper grid voltage sag conditions.

Currently, the LVRT standard only focus on four types of grid faults: single-phase short-circuit fault; two-phase short-circuit fault; three-phase short-circuit fault; and interphase short-circuit fault, in which three-phase short-circuit fault has no active power backflow problem due to symmetrical voltage [15]. Since [22] has completely solved the active power backflow problem under single-phase and two-phase short-circuit fault conditions, this article focuses on the control strategy of suppressing active power backflow under interphase short-circuit fault condition. The main contributions are as follows.

1) A novel multiple specific harmonic zero-sequence voltages compensation strategy (MSHZSVCS) is proposed for minimizing the amplitude of three-phase modulation voltages and then significantly shrinking active power backflow zone during interphase short-circuit fault.
2) The area of the active power backflow zones for different control methods are quantitatively calculated and compared by adopting polynomial fitting, adequately showing the advantages of the proposed method, that is, the inverter can operate stably under lower output power and smaller drop depth compared existing method, and improve the LVRT capability of the PV system.

The rest of this article is organized as follows: the active power backflow zone during interphase short-circuit fault by adopting ZSVCS is analyzed in Section II. On this basis, the MSHZSVCS is proposed in Section III. Then, by adopting the polynomial fitting, the active power backflow zone of different control methods is quantitatively calculated and compared in Section IV. Experimental results are presented to validate the performance of the proposed method in Section V. Finally, Section VI concludes this article.

II. Active Power Backflow Zone Analysis of ZSVCS

A. Topology Description

The topology structure of three-phase common dc-bus isolated CHB PV grid-connected inverter is shown in Fig. 1, where phase A, phase B, and phase C are composed of N modules and all modules have the same circuit structures. All modules all consist of single-input-four-output *LLC* converter connected with four HBs to simplify system communication design and improve the power density and efficiency, and the turns ratio of high-frequency transformer is N_T:1:1:1:1. The input ports of all modules are connected in parallel to generate a common dc bus, which connects multiple boost converters to achieve the maximum power point tracking of PV arrays. The output ports all modules form three serial strings connected to medium-voltage grid through three inductors L_f. As shown in Fig. 1, u_{gA}, u_{gB}, u_{gC} denote three-phase grid voltages; i_{gA}; i_{gB}; and i_{gC} denote three-phase grid currents; U_{HXij} denote the jth HB dc-bus voltage of ith module in phase X, $X = A,B,C$, $i = 1, 2, \ldots N$, $j = 1,2,3,4$; and u_{XT} denote the ac output voltages of CHB inverter in phase X.

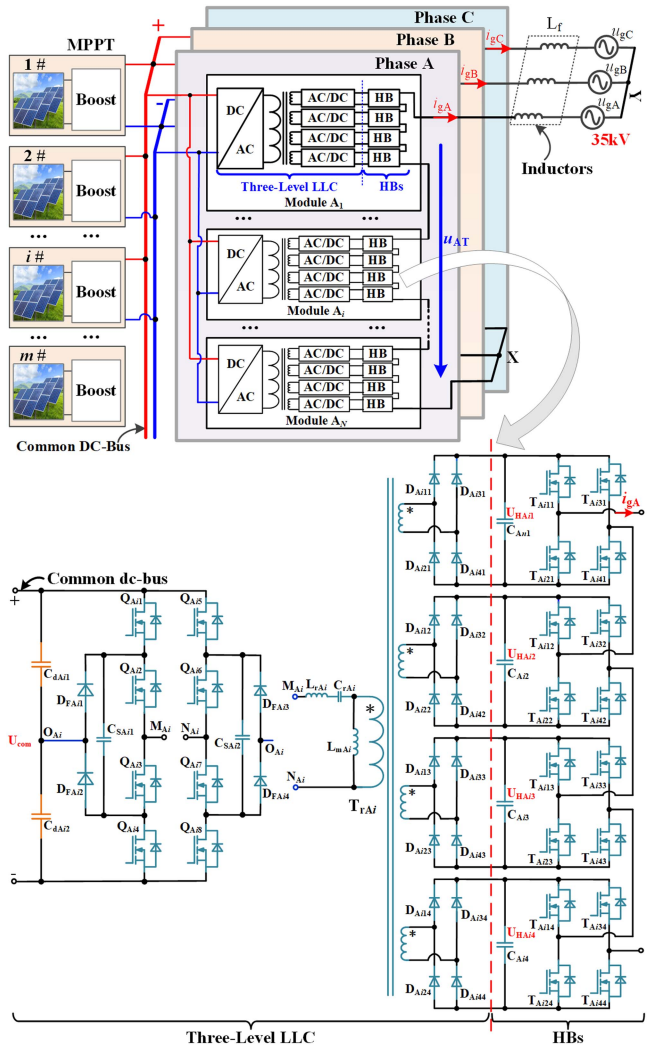

Fig. 1. Schematic diagram of three-phase common DC-bus isolated CHB PV grid-connected inverter.

B. LVRT Standard

Generally, although LVRT standards vary slightly in different countries, they all require the inverter to support the grid voltage by injecting reactive power. Taking the LVRT standard in China as an example, the amplitude of positive-sequence reactive current I_{qP}^* should track the voltage change at the point of common coupling in real time, as follows:

$$I_{qP}^* = \mathrm{K}_1 \times (0.9 - D) \times I_{gN}, \quad D < 0.9 \tag{1}$$

where K_1 is usually set to 2; I_{gN} enotes the rated amplitude of grid current; D denotes grid voltage drop depth, which is the ratio of line-voltage amplitude after and before voltage sag. In addition, the standard also requires that when an asymmetrical fault occurs, the value of I_{qP}^* should not exceed $0.4\ I_{gN}$.

Therefore, when the asymmetric interphase short-circuit fault occurs and I_{qP}^* is calculated as follows:

$$I_{qP}^* = \min\{2 \times (0.9 - D) I_{gN}, 0.4 I_{gN}\} \quad , D < 0.9\ . \tag{2}$$

TABLE I
U_{dP}, U_{qP}, U_{dN}, U_{qN}, AND β DURING INTERPHASE SHORT-CIRCUIT FAULT

	A-B	A-C	B-C
u_{dP}	$(D+1)\mathrm{U}_{\mathrm{gN}}/2$	$(D+1)\mathrm{U}_{\mathrm{gN}}/2$	$(D+1)\mathrm{U}_{\mathrm{gN}}/2$
u_{qP}	0	0	0
u_{dN}	$(D-1)\mathrm{U}_{\mathrm{gN}}/4$	$(D-1)\mathrm{U}_{\mathrm{gN}}/4$	$(1-D)\mathrm{U}_{\mathrm{gN}}/2$
u_{qN}	$\sqrt{3}(1-D)\mathrm{U}_{\mathrm{gN}}/4$	$\sqrt{3}(D-1)\mathrm{U}_{\mathrm{gN}}/4$	0
β	$2\pi/3$	$-2\pi/3$	0

The positive-sequence active current I_{qP}^* during LVRT is limited by two constraints: one is the maximum continuous output positive-sequence active current allowed by the converter I_{dP1}^*, the other is the positive-sequence active current that the converter is able to actually output I_{dP2}^*.

PV inverter is usually designed with 1.1 times overload capacity, that is, the maximum continuous output current is $1.1\mathrm{I}_{\mathrm{gN}}$, so I_{dP1}^* can be calculated as

$$I_{dP1}^* = \sqrt{(1.1 I_{gN})^2 - \left(I_{qP}^*\right)^2}. \tag{3}$$

To calculate I_{dP2}^* , the *d–q* axis components of the positive-sequence voltages, u_{dP}, u_{qP}, the *d–q* axis components of the negative-sequence voltage, u_{dN}, u_{qN}, the initial phase angle β of negative-sequence grid voltages, are calculated and summarized in Table I, where U_{gN} denotes the rated amplitude of grid phase voltages.

Define three variables, P_N, P_T, and $\mathrm{R_P}$, which denote the rated power, the total output power of PV arrays, the ratio of P_T and P_N, respectively, and then

$$P_T = 3 u_{dP} I_{dP2}^*/2, \quad P_N = 3 U_{gN} I_{gN}/2, \quad R_P = P_T/P_N\ . \tag{4}$$

By referring Table I and substituting u_{dP} into (4), I_{dP2}^* is calculated as follows:

$$I_{dP2}^* = 2 R_P I_{gN}/(D+1). \tag{5}$$

To prevent large active power shortage in ac grid, maximize energy harvest of the PV power station, and meet the overcurrent limitation, I_{dP}^* is calculated as

$$I_{dP}^* = \min\left\{I_{dP1}^* \quad , I_{dP2}^* \right\}. \tag{6}$$

C. Active Power Backflow Zone Analysis

The core idea of ZSVCS in [21] is to inject appropriate fundamental-frequency zero-sequence voltage so that it will completely offset the redistribution of negative-sequence voltage to three-phase active power, and then active power backflow can be avoided. The zero-sequence voltage to be compensated is

$$u_0 = \sqrt{(u_{dN})^2 + (u_{qN})^2}\cos(\omega t + \theta_1), \qquad \theta_1 = \beta + 2\varphi - \pi \tag{7}$$

where u_{dN}, u_{qN}, and β can be obtained based on Table I; φ denotes the power factor angle of CHB PV grid-connected inverter during LVRT and is calculated as follows:

$$\varphi = \arctan\left(\mathrm{I}_{qP}^*/\mathrm{I}_{dP}^*\right). \tag{8}$$

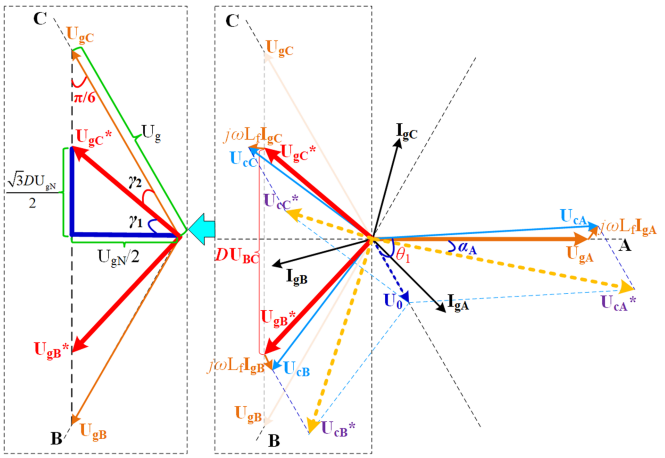

Fig. 2. Phasor diagram of interphase short-circuit fault between phase B and C by adopting ZSVCS.

To analyze the active backflow zone by adopting ZSVCS under interphase short-circuit fault condition, it is first necessary to calculate the amplitudes of the three-phase modulation voltage after adding u_0. During interphase short-circuit fault, the grid voltages of phases B and C are denoted as u_{gB}^* and u_{gC}^*, respectively. u_{cA}, u_{cB}, and u_{cC} denote the three-phase modulation voltages before adding u_0 and u_{cA}^*, u_{cB}^*, and u_{cC}^* denote the three-phase modulation voltages after u_0 compensated. Since the output voltages of three-phase isolated CHB PV inverter have a large number of levels, so the filter inductor is smaller and the inductor voltage is relatively low, which can be temporarily ignored. Then, u_{cA}^*, u_{cB}^*, and u_{cC}^* are as follows:

$$\begin{cases} u_{cA}^* = u_{cA} + u_0 \approx u_{gA} + u_0 \\ u_{cB}^* = u_{cB} + u_0 \approx u_{gB}^* + u_0 \\ u_{cC}^* = u_{cC} + u_0 \approx u_{gC}^* + u_0 \end{cases}. \tag{9}$$

The phasor diagram of interphase short-circuit fault of phases B and C by adopting ZSVCS is shown in Fig. 2, while the phasor diagram before compensating zero-sequence voltage is represented by the solid line. The three-phase modulation voltage amplitudes $||\mathbf{U_{cA}^*}||$, $||\mathbf{U_{cB}^*}||$, and $||\mathbf{U_{cC}^*}||$ after adopting ZSVCS are calculated as follows:

$$\begin{cases} \|\mathbf{U_{cA}^*}\|^2 \approx \|\mathbf{U_{gA}}\|^2 + \|\mathbf{U_0}\|^2 - 2\|\mathbf{U_{gA}}\|\|\mathbf{U_0}\|\cos(\pi - \theta_1) \\ = \left[1 + \left(\frac{1-D}{2}\right)^2 - 2\frac{1-D}{2}\cos(2\varphi)\right] \mathrm{U}_{gN}^2 \\ \|\mathbf{U_{cB}^*}\|^2 \approx \|\mathbf{U_{gB}^*}\|^2 + \|\mathbf{U_0}\|^2 - 2\|\mathbf{U_{gB}^*}\|\|\mathbf{U_0}\|\cos\left(\frac{\pi}{3} - \theta_1 - \gamma_2\right) \\ = \left[\frac{3D^2+1}{4} + \left(\frac{1-D}{2}\right)^2 - \sqrt{3D^2+1}\frac{1-D}{2}\cos\left(\frac{\pi}{3} - \theta_1 - \gamma_2\right)\right] \mathrm{U}_{gN}^2 \\ \|\mathbf{U_{cC}^*}\|^2 \approx \|\mathbf{U_{gC}^*}\|^2 + \|\mathbf{U_0}\|^2 - 2\|\mathbf{U_{gC}^*}\|\|\mathbf{U_0}\|\cos\left(\frac{\pi}{3} + \theta_1 - \gamma_2\right) \\ = \left[\frac{3D^2+1}{4} + \left(\frac{1-D}{2}\right)^2 - \sqrt{3D^2+1}\frac{1-D}{2}\cos\left(\frac{\pi}{3} + \theta_1 - \gamma_2\right)\right] \mathrm{U}_{gN}^2 \end{cases} \tag{10}$$

where γ_2 is calculated as

$$\gamma_2 = \pi/3 - \gamma_1 = \pi/3 - \arctan\left(\sqrt{3}D\right). \tag{11}$$

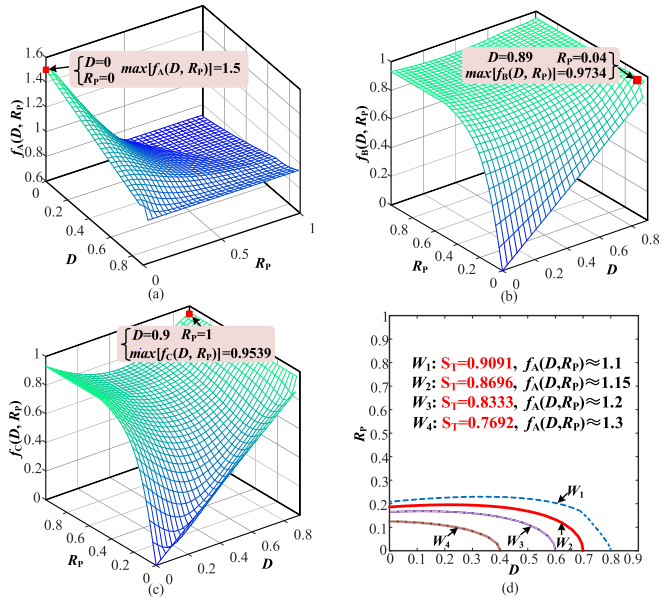

Fig. 3. Analysis results of ZSVCS. (a) $f_A(D, R_P)$. (b) $f_B(D, R_P)$. (c) $f_C(D, R_P)$. (d) Active power backflow zone at different modulation indexes.

Then, three functions $f_A(D, R_P)$, $f_B(D, R_P)$, and $f_C(D, R_P)$ are defined to denote the ratios of $||\mathbf{U_{cA}^*}||$, $||\mathbf{U_{cB}^*}||$, and $||\mathbf{U_{cC}^*}||$ to U_{gN}, respectively, shown as

$$\begin{cases} f_A(D, R_P) = \|\mathbf{U_{cA}^*}\|/\mathrm{U}_{gN} = \sqrt{1 + \left(\frac{1-D}{2}\right)^2 - 2\frac{1-D}{2}\cos(2\varphi)} \\ f_B(D, R_P) = \|\mathbf{U_{cB}^*}\|/\mathrm{U}_{gN} \\ = \sqrt{\frac{3D^2+1}{4} + \left(\frac{1-D}{2}\right)^2 - \sqrt{3D^2+1}\frac{1-D}{2}\cos\left(\frac{\pi}{3} - \theta_1 - \gamma_2\right)} \\ f_C(D, R_P) = \|\mathbf{U_{cC}^*}\|/\mathrm{U}_{gN} \\ = \sqrt{\frac{3D^2+1}{4} + \left(\frac{1-D}{2}\right)^2 - \sqrt{3D^2+1}\frac{1-D}{2}\cos\left(\frac{\pi}{3} + \theta_1 - \gamma_2\right)} \end{cases}. \tag{12}$$

The diagrams of $f_A(D, R_P)$, $f_B(D, R_P)$, and $f_C(D, R_P)$ are shown in Fig. 3(a)–(c). As could be seen, if interphase short-circuit fault between phases B and C occurs, the modulation voltage of phase A may be overmodulation. When $R_P = 0$ and $D = 0$, $f_A(D, R_P) = 1.5$, that is to say, the modulation voltage amplitude of phase A will reach 1.5 times of the rated value of grid voltage.

Since phase A may be overmodulation, the modulation index of three-phase common dc-bus isolated CHB PV grid-tied inverter is defined as follows:

$$\mathrm{S}_T = \frac{\mathrm{U}_{gN}}{\sum_{i=1}^{n}\sum_{j=1}^{4}\mathrm{U}_{HXij}} = \frac{\mathrm{U}_{gN}}{\|\mathbf{U_{cA}^*}\|}\frac{\|\mathbf{U_{cA}^*}\|}{\sum_{i=1}^{n}\sum_{j=1}^{4}\mathrm{U}_{HXij}}, \quad X = A, B, C. \tag{13}$$

Based on the operation principle of inverter, if (14) works, the inverter will be overmodulation

$$\|\mathbf{U_{cA}^*}\| \Big/ \sum_{i=1}^{n}\sum_{j=1}^{4}\mathrm{U}_{HXij} > 1. \tag{14}$$

Based on (12) ∼ (14), the overmodulation zone is as follows:

$$f_A(D,R_P)=\frac{\|\mathbf{U}^*_{\mathbf{cA}}\|}{\mathrm{U}_{gN}}=\sqrt{1+\left(\frac{1-D}{2}\right)^2-2\frac{1-D}{2}\cos(2\varphi)}>1/S_T. \tag{15}$$

As could be seen, the zone surrounded by curve $f_A(D, R_P) = 1/S_T$ and coordinate axes is the overmodulation zone, in which the three-phase common dc-bus isolated CHB PV grid-tied inverter may not operate normally due to seriously distorted grid current [7], [23], so the active power backflow is unable to effectively be solved. Therefore, when ZSVCS is adopted, the overmodulation zone can be regarded as the active power backflow zone under interphase short-circuit fault condition. Taking $S_T = 0.9091$, 0.8696, 0.8333, and 0.7692 as examples, draw the curve of $f_A(D, R_P) = 1/S_T$, which are curves W_1,W_2, W_3 and W_4, respectively, show in Fig. 3(d). With the decrease of S_T, the active power backflow zone of the three-phase common dc-bus isolated CHB PV grid-tied inverter will also decrease.

III. Multiple Specific Harmonic Voltages Compensation Strategy

Generally, the modulation index of PV inverter should not be too small in practical applications (not less than 0.8), that is, shrinking active power backflow zone only by reducing the modulation index of three-phase common dc-bus isolated CHB PV grid-tied inverter is not feasible. Therefore, this section proposes a MSHZSVCS to deal with this problem.

A. Multiple Harmonic Compensation Analysis

For sinusoidal modulation waveform u_{r1}, it is assumed that its amplitude is S, angular frequency is ω, and initial phase angle is α. After compensating odd harmonics, the total modulation waveform u_{rT} is obtained as follows:

$$u_{rT}=S\times\cos(\omega t+\alpha)+\sum_{i=1}^{n}C_k\times S\times\cos\left[k\left(\omega t+\alpha\right)\right],\quad k=2i+1 \tag{16}$$

where n is the number of the compensated harmonics, and C_k is compensation coefficient of the kth harmonic.

To avoid overmodulation, the amplitude of u_{rT} should not exceed 1, that is, the maximum of u_{rT} is not be greater than 1

$$\max(u_{rT})=S\max\left\{\cos(\omega t+\alpha)+\sum_{i=1}^{n}C_k\times\cos[k\left(\omega t+\alpha\right)]\right\}\le 1 \tag{17}$$

that is

$$S\le g\left(C_k\right)=\frac{1}{\max\{\cos(\omega t+\alpha)+\sum_{i=1}^{n}C_k\times\cos[k\left(\omega t+\alpha\right)]\}}. \tag{18}$$

The larger the value of S, the stronger the ability to avoid overmodulation after harmonic compensation. The maximum of $g(C_k)$, $\max[g(C_k)]$, is the maximum that S can obtain. Therefore, for reducing the amplitude of u_{rT} to the maximum extent and obtaining the maximum overmodulation suppression capability, the compensation coefficient of each harmonic must be determined, that is, the value of C_k. Since $g(C_k)$ is a multivariate nonlinear transcendental function, C_k and $\max[g(C_k)]$ are calculated by MATLAB, which is given in Table II.

TABLE II
Maximum of $g(C_k)$ and C_k Under Different Number of Harmonic

n	C_3	C_5	C_7	C_9	C_{11}	C_{13}	$\max[g(C_k)]$
1	0.1667	0	0	0	0	0	1.155
2	0.2316	0.06	0	0	0	0	1.207
3	0.265	0.1	0.029	0	0	0	1.231
4	**0.285**	**0.13**	**0.06**	**0.02**	**0**	**0**	**1.2438**
5	0.295	0.14	0.07	0.03	0.01	0	1.2499
6	0.3	0.15	0.085	0.045	0.02	0.005	1.2528

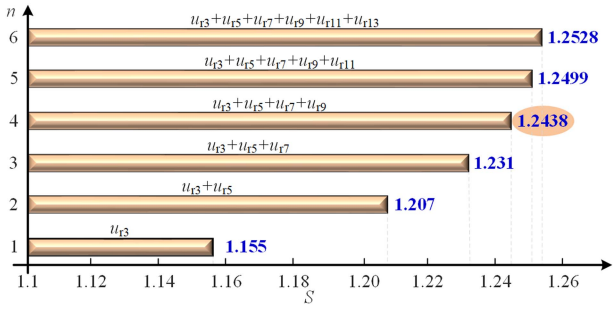

Fig. 4. Maximum value of S when compensating different harmonics.

In summary, if C_k is adopted based on Table II, the maximum value of S is obtained on the premise of avoiding overmodulation, shown in Fig. 4. As the number of harmonic increases, the value of S will gradually increase, that is, although the amplitude of modulation waveform u_{r1} is larger, the amplitude of u_{rT} is not greater than 1 by compensating reasonable harmonics, meaning that the ability to suppress overmodulation is enhanced. In addition, according to Fig. 4, when n is less than or equal to 4, S increases significantly with the increase of n; when n is greater than 4, S increases slowly. Considering the overmodulation suppression capability and the computational complexity, $n = 4$ is considered in this article, that is, the third, fifth, seventh, and ninth harmonics are reasonably compensated. When different harmonics compensated, the waveform diagrams are shown in Fig. 5. As could be seen, the modulation waveform amplitude is able to be reduced from 1.2438 to 1 after compensating the third, fifth, seventh, and ninth harmonics according to Table II, consistent with the above theoretical analysis.

B. Multiple Specific Harmonic Zero-Sequence Voltages Compensation Strategy

If interphase short-circuit fault between phase B and C occurs, the angle α_A between $\mathbf{U}^*_{\mathbf{cA}}$ and $\mathbf{U}_{\mathbf{gA}}$ satisfies the following expression based on Fig. 2

$$\cos\left(\alpha_A\right)\approx\frac{\|\mathbf{U}_{\mathbf{gA}}\|^2+\|\mathbf{U}^*_{\mathbf{cA}}\|^2-\|\mathbf{U}_{\mathbf{0}}\|^2}{2\|\mathbf{U}_{\mathbf{gA}}\|\|\mathbf{U}^*_{\mathbf{cA}}\|}$$

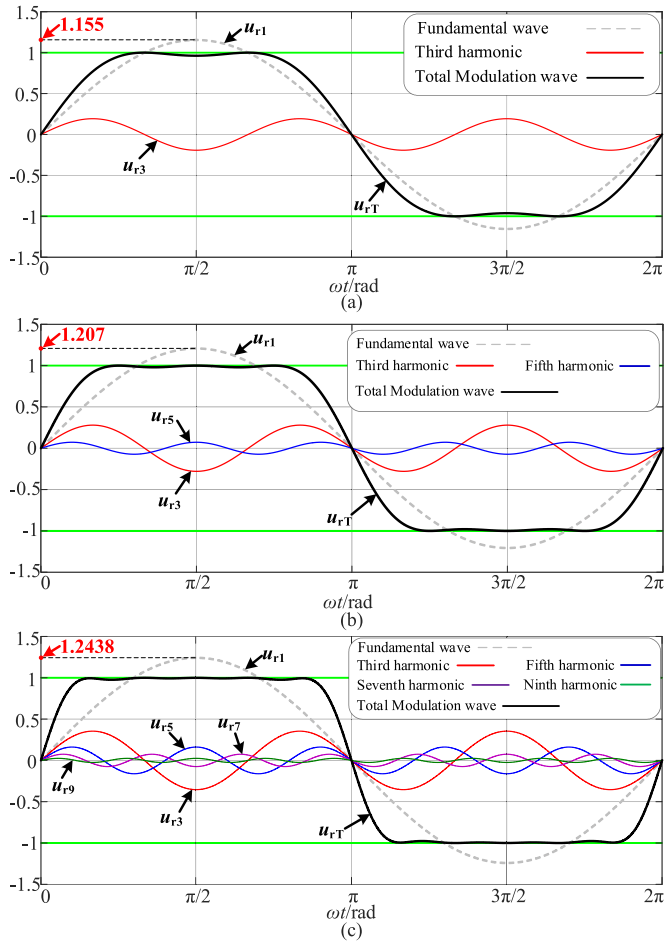

Fig. 5. Waveform diagrams when different harmonics compensated. (a) Third harmonic. (b) Third and fifth harmonics. (c) Third, fifth, seventh, and ninth harmonics.

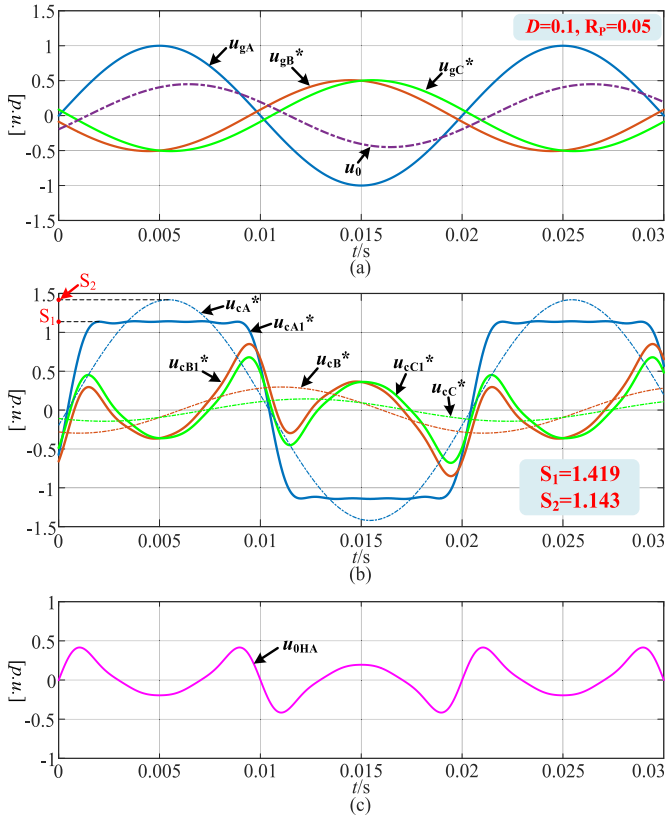

Fig. 6. Output waveforms when interphase short-circuit fault between phase B and phase C occur. (a) u_{gA}, u^*_{gB}, u^*_{gC}, and u_0. (b) u^*_{cA}, u^*_{cB}, u^*_{cC}, and u^*_{cA1}, u^*_{cB1}, u^*_{cC1}. (c) $u_{0\mathrm{HA}}$.

$$= \frac{2-(1-D)\cos(2\varphi)}{\sqrt{4+(1-D)^2-4(1-D)\cos(2\varphi)}}. \quad (19)$$

Since cosine function is monotone function on [0, π], α_{A} is calculated as

$$\alpha_A = \arccos\left[\frac{2-(1-D)\cos(2\varphi)}{\sqrt{4+(1-D)^2-4(1-D)\cos(2\varphi)}}\right]. \quad (20)$$

According to (10) and (20), after compensating the zero-sequence voltage u_0, the analytical expression of u^*_{cA} is

$$u^*_{cA} = \|\mathbf{U}^*_{\mathbf{cA}}\|\cos(\omega t-\alpha_A) = \sqrt{1+\left(\frac{1-D}{2}\right)^2-(1-D)\cos(2\varphi)}\times \mathrm{U}_{gN}\cos(\omega t-\alpha_A). \quad (21)$$

Based on Fig. 3, only the modulation voltage amplitude of the non-fault phase (phase A) will significantly increase after compensating u_0, while the modulation voltage amplitude of the other two phase (phases B and C) will decrease. For lowering the modulation voltage amplitude of the phase A, If $n = 4$, the total harmonic voltages to be compensated is calculated as follows:

$$u_{0HA} = \mathrm{U}_{gN}\sqrt{1+\left(\frac{1-D}{2}\right)^2-(1-D)\cos(2\varphi)} \times \sum_{k=3,5,7,9} C_k\cos(k\omega t-k\alpha_A) \quad (22)$$

where $C_3 = 0.285$, $C_5 = 0.13$, $C_7 = 0.06$, $C_9 = 0.02$.

Since the studied topology is a three-phase star-connected inverter, u_{0HA} will be simultaneously compensated to three-phase modulation voltages as zero-sequence voltage to avoid injecting harmonic current into the power grid [7]. After compensating $u_{0\mathrm{HA}}$ for u^*_{cA}, u^*_{cB}, and u^*_{cC}, the final three-phase modulation voltages u^*_{cA1}, u^*_{cB1}, and u^*_{cC1} are as follows:

$$\begin{cases} u^*_{cA1}(D,R_P,\omega t) = u^*_{\mathrm{cA}} + u_{0HA} \approx u_{gA}+u_0+u_{0HA} \\ u^*_{cB1}(D,R_P,\omega t) = u^*_{\mathrm{cB}} + u_{0HA} \approx u^*_{gB}+u_0+u_{0HA} \\ u^*_{cC1}(D,R_P,\omega t) = u^*_{\mathrm{cC}} + u_{0HA} \approx u^*_{gC}+u_0+u_{0HA} \end{cases}. \quad (23)$$

However, although injecting harmonic zero-sequence voltage u_{0HA} can reduce the modulation voltage amplitude of phase A, it must increase the modulation voltage amplitudes of phase B and C to a certain extent. Taking $D = 0.1$ and $R_P = 0.05$ as an example, the output waveforms are shown in Fig. 6 when interphase short-circuit fault between phase B and phase C occurs.

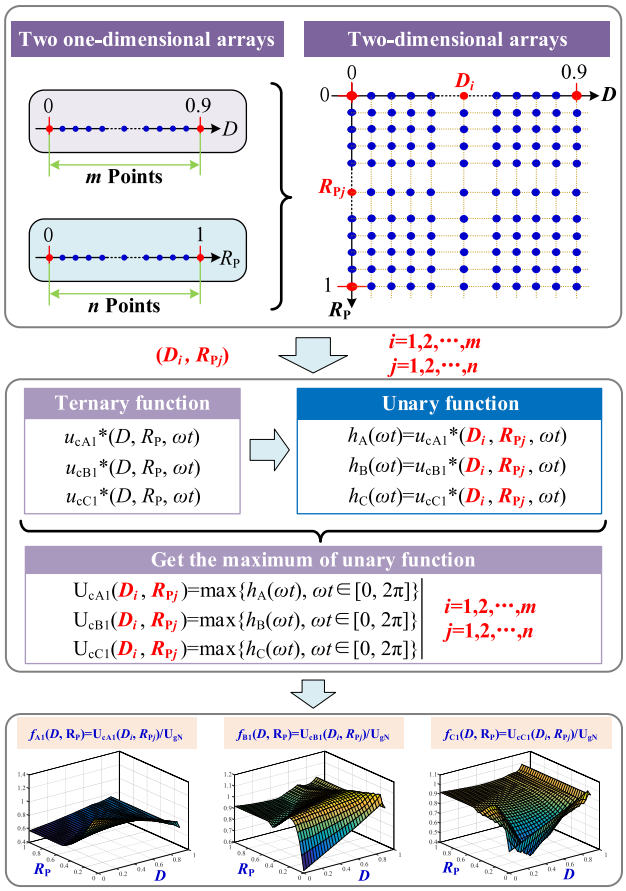

Fig. 7. Graphic analysis method for obtaining the amplitudes of u^*_{cA1}, u^*_{cB1}, and u^*_{cC1}.

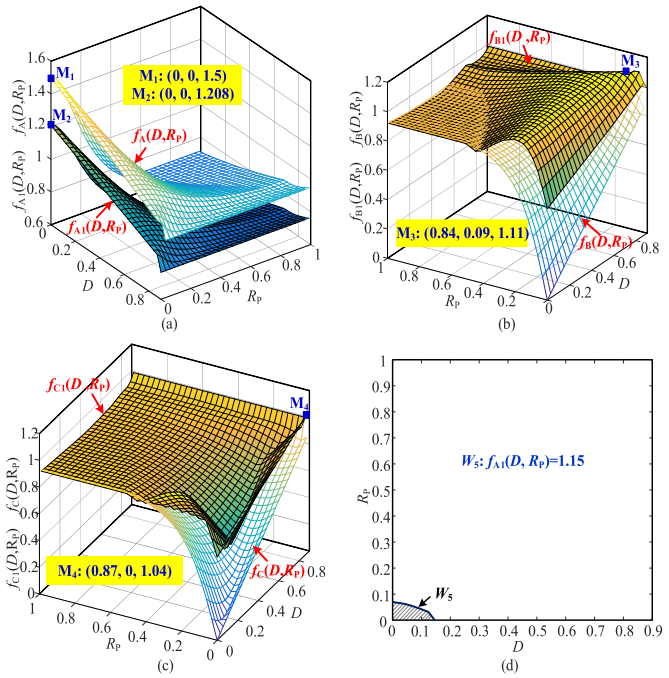

Fig. 8. Analysis results of the proposed MSHZSVCS. (a) $f_A(D, R_P)$, $f_{A1}(D, R_P)$. (b) $f_B(D, R_P)$, $f_{B1}(D, R_P)$. (c) $f_C(D, R_P)$, $f_{C1}(D, R_P)$. (d) Active power backflow zone.

All variables are expressed in per-unit (p.u.) value, that is, their actual values are divided by U_{gN}. After interphase short-circuit fault, three-phase grid voltages, u_{gA}, u^*_{gB}, u^*_{gC}, and the compensated zero-sequence voltage u_0 are given in Fig. 6(a). If the ZSVCS is adopted, three-phase modulation voltages u^*_{cA}, u^*_{cB}, u^*_{cC} are shown in Fig. 6(b). For comparison, if the proposed MSHZSVCS is adopted, three-phase modulation voltages, u^*_{cA1}, u^*_{cB1}, u^*_{cC1}, are also shown in Fig. 6(b), and the added multiple harmonic u_{0HA} is shown in Fig. 6(c). As could be seen, after u_{0HA} is added, the modulation voltage amplitude of phase A decreases from 1.419 to 1.143. The modulation voltage amplitudes of phase B and C will increase, but not more than 1.

Since the modulation voltage amplitudes of phases B and C will increase, it is necessary to analyze the amplitude of u^*_{cA1}, u^*_{cB1}, u^*_{cC1} in the whole operating range to determine the active power backflow zone when using the proposed control method. Considering that u^*_{cA1}, u^*_{cB1}, and u^*_{cC1} contain harmonic components, which cannot be analyzed by phasor method, graphical method is adopted in time domain with the help of MATLAB to simplify the analysis, as shown in Fig. 7. First, evenly select m points on the interval $D\in[0, 0.9]$ and n points on the interval $R_P\in[0, 1]$ to form a two-dimensional (2-D) array (D_i, R_{Pj}), $i = 1,2,\ldots,m$, $j = 1,2,\ldots,n$. Secondly, (D_i, R_{Pj}) is introduced into (23), the ternary functions $u^*_{cA1}(D, R_P, \omega t)$, $u^*_{cB1}(D, R_P, \omega t)$, and u^*_{cC1} $(D, R_P, \omega t)$ become the univariate functions $h_A(\omega t)$, $h_B(\omega t)$, $h_C(\omega t)$. Thirdly, for each point (D_i, R_{Pj}), find the maximum values of $h_A(\omega t)$, $h_B(\omega t)$, $h_C(\omega t)$ in the interval $\omega t\in[0, 2\pi]$, and denoted as $U_{cA1}(D_i, R_{Pj})$, $U_{cB1}(D_i, R_{Pj})$ and $U_{cC1}(D_i, R_{Pj})$, respectively. Obviously, $U_{cA1}(D_i, R_{Pj})$, $U_{cB1}(D_i, R_{Pj})$ and $U_{cC1}(D_i, R_{Pj})$ represent the maximum values of u^*_{cA1}, u^*_{cB1}, and u^*_{cC1} in the range of $D\in[0, 0.9]$ and $R_P\in[0, 1]$. Fourthly, three functions $f_{A1}(D, R_P)$, $f_{B1}(D, R_P)$ and $f_{C1}(D, R_P)$, are defined to represent the ratio of $U_{cA1}(D_i, R_{Pj})$, $U_{cB1}(D_i, R_{Pj})$, and $U_{cC1}(D_i, R_{Pj})$ to U_{gN}, given in (24). Finally, the 3-D diagrams of $f_{A1}(D, R_P)$, $f_{B1}(D, R_P)$, and $f_{C1}(D, R_P)$ can be plotted.

$$\begin{cases} f_{A1}(D, R_P) = U_{cA1}(D_i, R_{Pj})/U_{gN} \\ f_{B1}(D, R_P) = U_{cB1}(D_i, R_{Pj})/U_{gN} \\ f_{C1}(D, R_P) = U_{cC1}(D_i, R_{Pj})/U_{gN} \end{cases} \quad \begin{matrix} i = 1, 2, \ldots, m \\ j = 1, 2, \ldots, n \end{matrix} . \tag{24}$$

The 3-D diagrams of $f_A(D, R_P)$, $f_{A1}(D, R_P)$, $f_B(D, R_P)$, $f_{B1}(D, R_P)$, $f_C(D, R_P)$, and $f_{C1}(D, R_P)$ are shown in Fig. 8(a)–(c). As could be seen, after adopting the proposed control method, the modulation voltage amplitude of phase A decreases obviously in the whole operating zone, and the maximum value is reduced from 1.5 to 1.208. Although the modulation voltage amplitudes of phases B and C will increase within a certain range, they do not exceed 1.155. Taking $S_T = 0.8696$ as an example ($1/S_T = 1.15$), neither phase B nor phase C will be overmodulation, so the active power backflow zone is still determined by phase A. According to (13), (14), and (24),

the active power backflow zone is obtained as follows:

$$f_{A1}(D, R_P) = U_{cA1}(D_i, R_{Pj})/U_{gN} > 1/S_T. \quad (25)$$

Then, draw the active power backflow zone of the three-phase common dc-bus isolated CHB PV grid-connected inverter, which is the area surrounded by W_5 ($f_{A1}(D, R_P) = 1.15$) and coordinate axes D and R_P, shown in Fig. 8(d).

Considering the rotation symmetry of three phases, if interphase short-circuit fault between phase A and C occurs and the fundamental-frequency zero-sequence voltage of (7) is injected, phase B will be overmodulation. Under this working scenario, the angle between $\mathbf{U^*_{cB}}$ and $\mathbf{U_{gB}}$ is denoted as α_B, and the multiple harmonic zero-sequence voltage compensated is denoted as u_{0HB}. If interphase short-circuit fault between phases A and B occurs and the fundamental-frequency zero-sequence voltage of (7) is injected, phase C will be overmodulation. The angle between $\mathbf{U^*_{cC}}$ and $\mathbf{U_{gC}}$ is denoted as α_C, and the multiple harmonic zero-sequence voltage compensated is denoted as u_{0HC}. Based on (19) and (20), α_B and α_C are calculated as follows:

$$\alpha_B = \alpha_C = \arccos\left[\frac{2-(1-D)\cos(2\varphi)}{\sqrt{4+(1-D)^2-4(1-D)\cos(2\varphi)}}\right]. \quad (26)$$

To lower the modulation voltage amplitude of phase B during interphase short-circuit between phases A and C, u_{0HB} is calculated as

$$\begin{aligned} u_{0HB} &= \|\mathrm{U}^*_{cB}\| \sum_{k=3,5,7,9} C_k \cos\left[k\left(\omega t - \frac{2\pi}{3} - \alpha_B\right)\right] \\ &= U_{gN}\sqrt{1+\left(\frac{1-D}{2}\right)^2 - (1-D)\cos(2\varphi)} \\ &\quad \times \sum_{k=3,5,7,9} C_k \cos\left[k\left(\omega t - \frac{2\pi}{3} - \alpha_B\right)\right]. \end{aligned} \quad (27)$$

To lower the modulation voltage amplitude of phase C during interphase short-circuit between phases A and B, u_{0HC} is calculated as

$$\begin{aligned} u_{0HC} &= \|U^*_{cC}\| \sum_{k=3,5,7,9} C_k \cos\left[k\left(\omega t + \frac{2\pi}{3} - \alpha_C\right)\right] \\ &= U_{gN}\sqrt{1+\left(\frac{1-D}{2}\right)^2 - (1-D)\cos(2\varphi)} \\ &\quad \times \sum_{k=3,5,7,9} C_k \cos\left[k\left(\omega t + \frac{2\pi}{3} - \alpha_C\right)\right]. \end{aligned} \quad (28)$$

Adopting the proposed MSHZSVCS, the flow chart of fundamental-frequency and harmonic zero-sequence voltages compensation is shown in Fig. 9. Therefore, no matter which interphase short-circuit fault occurs, the proposed control method is able to effectively reduce the active power backflow zone.

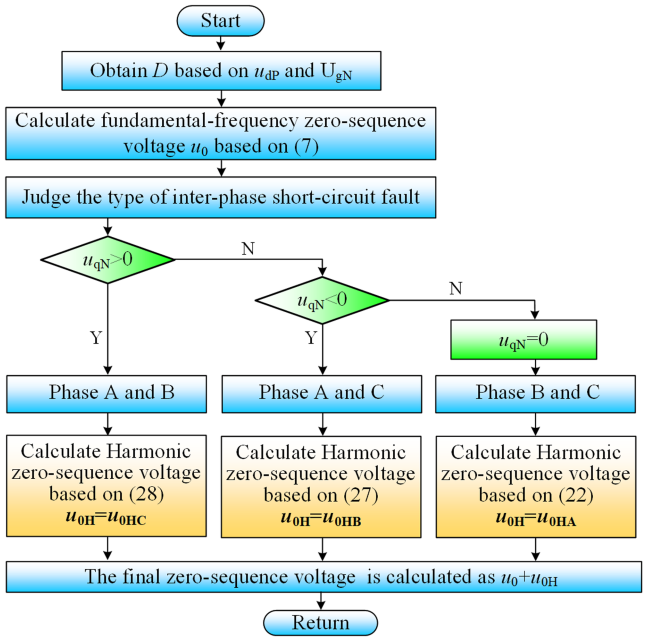

Fig. 9. Flow chart of multiple final zero-sequence voltage compensation.

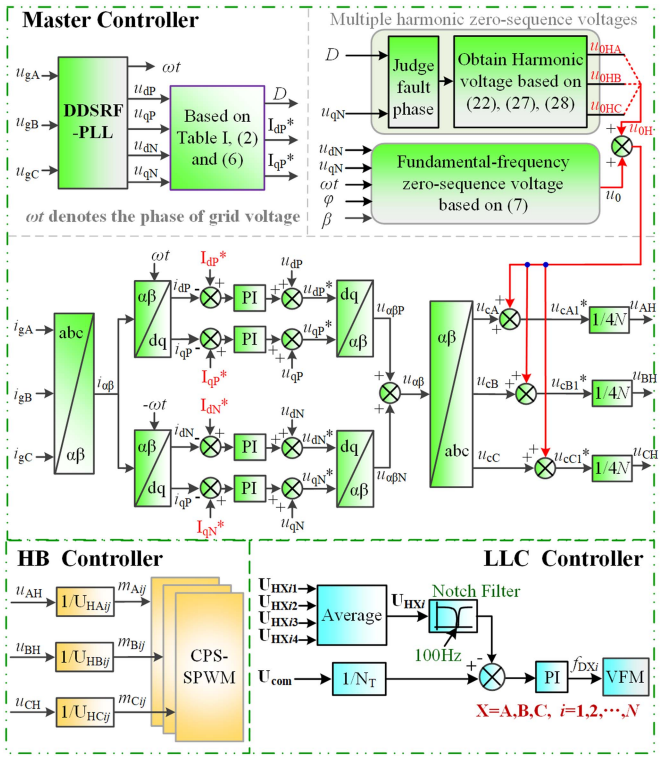

Fig. 10. Control block diagram of the proposed control strategy.

C. Control Strategy Implementation

The block diagram of the proposed control strategy is shown in Fig. 10, which is composed of master controller, HB controller and *LLC* controller. In master controller, the phase angle of the grid voltages ωt, fault type and drop depth D are obtained

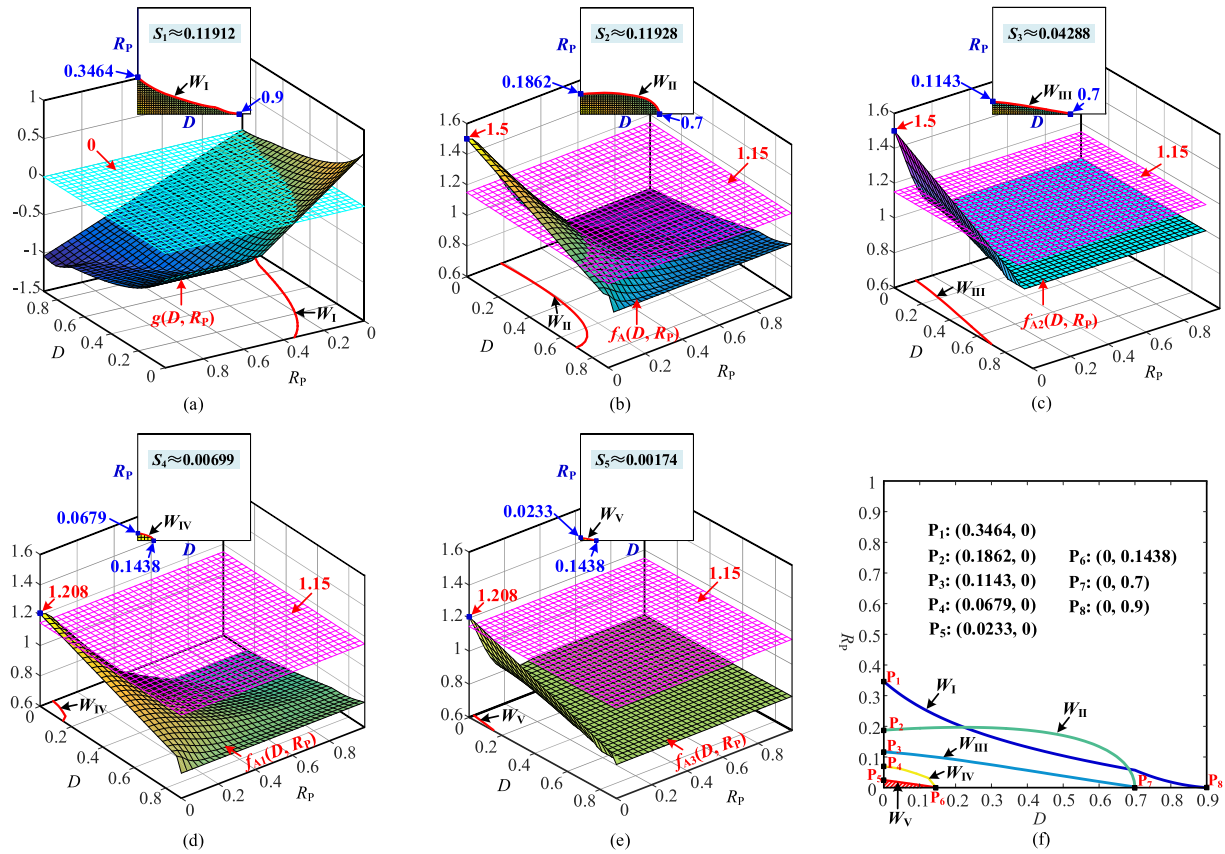

Fig. 11. Active power backflow zone and its area with different control methods. (a) Active current injection strategy. (b) Zero-sequence voltage compensation strategy. (c) Adaptive zero-sequence voltage compensation strategy. (d) Multiple specific harmonic zero-sequence voltages compensation strategy. (e) Combination control method of AZSVCS and MSHZSVCS. (f) Comparison of active power backflow zone.

based on decoupled double synchronous reference frame phase-locked loop [24], which can accurately check the grid status even if the grid voltages contain harmonics. Then, the positive-sequence active reference current I_{dP}^* and reactive reference current I_{qP}^*, fundamental-frequency zero-sequence voltage u_0 and multiple harmonic zero-sequence voltage u_{0H} is calculated. In addition, to achieve symmetrical three-phase grid currents, the negative-sequence active reference current I_{dN}^* and reactive reference current I_{qN}^* are both set to zero. The HB controllers calculate the modulation waveforms of all HB converters, and obtain switching driving signals through the carrier phase-shift sine pulsewidth modulation. *LLC* controllers is responsible for controlling the dc-bus average voltage of four HBs, and generating switching driving signals of three-level *LLC* converter by variable frequency modulation [25].

IV. Theoretical Comparison of Active Power Backflow Zone of Different Methods

This section compares the active power backflow zone when the existing ACIS [15], ZSVCS [21], AZSVCS [22], the proposed MSHZSVCS, and the combination control method of AZSVCS and MSHZSVCS are used, respectively. The area of active power backflow zone is calculated to quantify the performance of different control methods. That is, the smaller the area is, the stronger the ability to suppress active power backflow is.

A. Performance Analysis of ACIS

Referring to [15], for avoiding active power backflow under interphase short-circuit fault condition, the positive-sequence active current I_{dP}^* and positive-sequence reactive current I_{qP}^* must satisfy

$$I_{dP}^* \geq \frac{\sqrt{3}\,(1-D)}{3D+1} I_{qP}^*. \tag{29}$$

Based on (29), define the function $g(D, R_P)$ as follows:

$$g\,(D, R_P) = \left[\frac{\sqrt{3}\,(1-D)}{3D+1} I_{qP}^* - I_{dP}^*\right] \Big/ I_{gN}. \tag{30}$$

Draw the 3-D surface graph of $g(D, R_P)$ about D and R_P in MATLAB, as shown in Fig. 11(a), where curve W_{I} is the contour line with $g(D, R_P)$, and the expression of W_{I} in the D-R_P plane is

$$R_{P1}\,(D) = \begin{cases} \frac{\sqrt{3}\left(1-D^2\right)(0.9-D)}{3D+1}, & 0.7 \leq D < 0.9 \\ \frac{0.4\times\sqrt{3}\left(1-D^2\right)}{2(3D+1)}, & D < 0.7 \end{cases}. \tag{31}$$

Obviously, the zone enclosed by W_{I} and the coordinate axes D and R_P is the active power backflow zone when ACIS is adopted

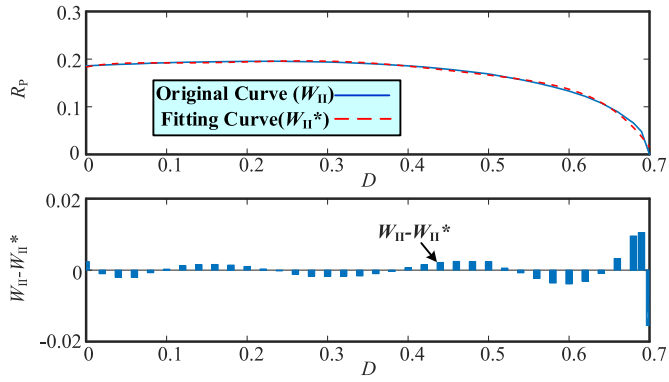

Fig. 12. Six-order curve fitting of W_{II} and residual.

under interphase short-circuit condition. To achieve quantitative analysis, the area of this zone, S_1, is calculated as follows:

$$S_1 = \int_0^{0.7} \frac{0.4\times\sqrt{3}\left(1-D^2\right)}{2\left(3D+1\right)}dD + \int_{0.7}^{0.9} \frac{\sqrt{3}\left(1-D^2\right)\left(0.9-D\right)}{3D+1}dD \approx 0.11912. \quad (32)$$

B. Performance Analysis of ZSVCS

Based on (12)–(14), when interphase short-circuit fault between phases B and C occurs and ZSVCS in [21] is adopted, the active power backflow zone is determined by (15), that is, $f_A(D, R_P)$>1/S_T. Taking $S_T = 0.8696$ (1/S_T = 1.15) as an example, the 3-D surface graph of $f_A(D, R_P)$, its contour line and active power backflow zone are drawn in MATLAB and shown in Fig. 11(b), where curve W_{II} is the contour line of $f_A(D, R_P) = 1/S_T$, and the expression of W_{II} in D-R_P plane is

$$\sqrt{1+\left(\frac{1-D}{2}\right)^2 - 2\frac{1-D}{2}\cos\left(2\varphi\right)} = \frac{1}{S_T}. \quad (33)$$

Obviously, the zone enclosed by W_{II} and coordinate axes D and R_P is the active power backflow zone. Since curve W_{II} is an implicit function, its explicit expression cannot be obtained directly. To calculate quantitatively its area, polynomial fitting of W_{II} is carried out. When using six-order curve fitting, the error can meet analysis requirements, shown in Fig. 12, where $W_{\mathrm{II}}*$ denotes the fitting curve, and its expression is

$$R_{P2}\left(D\right) = a_6D^6+a_5D^5+a_4D^4+a_3D^3+a_2D^2+a_1D+a_0 \quad (34)$$

where $a_6 = -71.096$, $a_5 = 132.29$, $a_4 = -92.953$, $a_3 = 30.035$, $a_2 = -4.5894$, $a_1 = 0.325$, and $a_0 = 0.1836$.

Then, the area S_2 of the zone enclosed by $W_{\mathrm{II}}*$ and coordinate axes D and R_{P} can be calculated as:

$$S_2 = \int_0^{0.7}\left(a_6D^6+a_5D^5+a_4D^4+a_3D^3+a_2D^2+a_1D+a_0\right)dD \approx 0.11928. \quad (35)$$

C. Performance Analysis of AZSVCS

Still taking interphase short-circuit fault between phases B and C as an example, when the AZSVCS in [22] is adopted, the zero-sequence voltage to be compensated is as

$$u_0 = q\times\frac{1-D}{2}U_{gN}\cos\left(\omega t+2\varphi-\pi\right) \quad (36)$$

where

$$\begin{cases} q \geq 1-\frac{2(D+1)I^*_{dP}}{(1-D)\left(I^*_{dP}+\sqrt{3}I^*_{qP}\right)}, & I^*_{dP} \geq \frac{\sqrt{3}(1-D)}{3D+1}I^*_{qP} \\ q = 0, & I^*_{dP} < \frac{\sqrt{3}(1-D)}{3D+1}\mathrm{I}^*_{qP} \end{cases}. \quad (37)$$

According to (12), (36) and (37), the ratio $f_{\mathrm{A2}}(D, R_P)$ of the modulation voltage amplitude of phase A, $\|\mathbf{U}^*_{\mathbf{cA2}}\|$, to U_{gN} is

$$f_{A2}\left(D,R_P\right) = \|\mathbf{U}^*_{\mathbf{cA2}}\|/U_{gN} = \sqrt{1+\left(q\frac{1-D}{2}\right)^2 - 2q\frac{1-D}{2}\cos\left(2\varphi\right)}. \quad (38)$$

Draw the 3-D diagram of $f_{A2}(D, R_P)$, contour line and active power backflow zone, which are shown in Fig. 11(c), where curve W_{III} is the contour line of $f_{A2}(D, R_P) = 1/S_T$ (1/S_T = 1.15), and the expression of W_{III} in D-$\mathrm{R_P}$ plane is

$$\sqrt{1+\left(q\frac{1-D}{2}\right)^2 - 2q\frac{1-D}{2}\cos\left(2\varphi\right)} = \frac{1}{S_T}. \quad (39)$$

Therefore, the zone enclosed by W_{III} and coordinate axes D and R_P is the active power backflow zone. To calculate quantitatively its area, polynomial fitting of W_{III} is carried out. When using the two-order curve fitting, the error can meet the engineering requirements, shown in Fig. 18 in the appendix, where $W_{\mathrm{III}}*$ denotes the fitting curve, and its expression is as

$$R_{P3}\left(D\right) = b_2D^2+b_1D+b_0 \quad (40)$$

where $b_2 = -0.0474$, $b_1 = -0.1357$, and $b_0 = 0.1165$

Then, the area S_3 of the zone enclosed by W_3* and coordinate axes D and R_P can be calculated as

$$S_3 = \int_0^{0.7}\left(b_2D^2+b_1D+b_0\right)dD \approx 0.04288. \quad (41)$$

D. Performance Analysis of MSHZSVCS

Based on (25), the 3-D surface graph of $f_{A1}(D, R_P)$, its contour line and active power backflow zone are shown in Fig. 11(d), where curve W_{IV} is the contour line of $f_{A1}(D, R_P) = 1/S_T$. The zone enclosed by W_{IV} and coordinate axes D and R_P is the active power backflow zone. Similarly, if using the six-order curve fitting, the error can meet engineering requirements, shown in Fig. 19 in the appendix, where $W_{\mathrm{IV}}*$ denotes the fitting curve, and its expression is

$$R_{P4}\left(D\right) = c_6D^6+c_5D^5+c_4D^4+c_3D^3+c_2D^2+c_1D+c_0 \quad (42)$$

where $c_6 = -158903$, $c_5 = 60355$, $c_4 = -8643.3$, $c_3 = 568.41$, $c_2 = -17.796$, $c_1 = 0.0239$, and $c_0 = 0.0684$.

Then, the area S_4 of the zone enclosed by $W_{\mathrm{IV}}*$ and coordinate axes D and R_{P} can be calculated as

$$S_4 = \int_0^{0.1438} \left(c_6D^6+c_5D^5+c_4D^4+c_3D^3+c_2D^2+c_1D+c_0\right) dD \approx 0.00699. \tag{43}$$

E. Performance Analysis of the Combination Control Method of AZSVCS and MSHZSVCS

Taking interphase short-circuit fault between phases B and C as an example, when the AZSVCS is adopted, the modulation voltage amplitude of phase A, $\|\mathbf{U}^*_{\mathbf{cA2}}\|$, and the angle between $\mathbf{U}^*_{\mathbf{cA2}}$ and $\mathbf{U}_{\mathbf{gA}}$, α_{A1}, are calculated as

$$\|\mathbf{U}^*_{\mathbf{cA2}}\| = \mathrm{U}_{gN}\sqrt{1+\left(q\frac{1-D}{2}\right)^2 - q\,(1-D)\cos(2\varphi)} \tag{44}$$

$$\alpha_{A1} = \arccos\left(\frac{2-q\,(1-D)\cos(2\varphi)}{\sqrt{4+q^2(1-D)^2-4q\,(1-D)\cos(2\varphi)}}\right). \tag{45}$$

Considering the compensation of the third, fifth, seventh and ninth harmonics to reduce the modulation voltage amplitude of phase A, the harmonic zero-sequence voltage to be injected can be calculated as

$$\begin{aligned} u_{0H} &= \|\mathbf{U}^*_{\mathbf{cA2}}\| \sum_{k=3,5,7,9} C_k\cos\left[k\left(\omega t-\alpha_{A1}\right)\right] \\ &= \mathrm{U}_{gN}\sqrt{1+\left(q\frac{1-D}{2}\right)^2 - q\,(1-D)\cos(2\varphi)} \\ &\quad\times \sum_{k=3,5,7,9} C_k\cos\left[k\left(\omega t-\alpha_{A1}\right)\right]. \end{aligned} \tag{46}$$

When the combined control method of AZSVCS and MSHZSVCS is adopted, the final zero-sequence voltage consists of two parts, one is adaptive fundamental-frequency zero-sequence voltage, and the other is multiple harmonic zero-sequence voltage. Therefore, the expression of the final zero-sequence voltage is

$$\begin{aligned} u_0^* &= q\times\frac{1-D}{2}U_{gN}\cos\left(\omega t+2\varphi-\pi\right) \\ &\quad + U_{gN}\sqrt{1+\left(q\frac{1-D}{2}\right)^2 - q\,(1-D)\cos(2\varphi)} \\ &\quad\times \sum_{k=3,5,7,9} C_k\cos\left[k\left(\omega t-\alpha_{A1}\right)\right]. \end{aligned} \tag{47}$$

Similarly, the modulation voltage amplitude of phase A, $\|\mathbf{U}^*_{\mathbf{cA3}}\|$, and the ratio of $\|\mathbf{U}^*_{\mathbf{cA3}}\|$ to U_{gN}, $f_{\mathrm{A3}}(D, R_P)$, are obtained by graphical method of Fig. 7. The 3-D surface graph of $f_{A3}(D, R_P)$, its contour line and active power backflow zone are shown in Fig. 11(e), where curve W_{V} is the contour line of $f_{A3}(D, R_P) = 1/S_T$ ($1/S_T = 1.15$). Therefore, the area enclosed by W_V and coordinate axes D and R_P is the active power backflow zone when the combination control method of AZSVCS and MSHZSVCS is adopted under interphase short-circuit fault condition. Then, if using the two-order curve fitting of W_V, the error can meet the engineering requirements, shown in Fig. 20 in the appendix, where $W_{V}*$ denotes the fitting curve, and its expression is as

$$R_{P5}(D) = d_2D^2+d_1D+d_0 \tag{48}$$

where $d_2 = -0.0861$, $d_1 = -0.1514$, and $d_0 = 0.0236$.

Then, the area S_5 of the zone enclosed by $W_{V}*$ and coordinate axes D and R_P can be calculated as:

$$S_5 = \int_0^{0.1438} \left(d_2D^2+d_1D+d_0\right) dD \approx 0.00174. \tag{49}$$

Put curves $W_{\mathrm{I}}\sim W_V$ in the same coordinate plane, and compare their active power backflow zone when different control methods are used, shown in Fig. 11(f). As could be seen, although the proposed MSHZSVCS still has a small active power backflow zone, it can be significantly reduced compared with the existing ACIS, ZSVCS and AZSVCS, and the combination control method of AZSVCS and MSHZSVCS has the optimal performance. In addition, when different control methods are adopted, the area of active power backflow zone are given in Table III. Compared with ACIS, the proposed MSHZSVCS is able to reduce active power backflow zone by 94.13%, and the combination control method of AZSVCS and MSHZSVCS is able to reduce active power backflow zone by 98.54%, which is recommended in practical application.

V. Experimental Results

A down-scaled experimental prototype of three-phase common dc-bus isolated CHB PV grid-connected inverter with two module of each phase (two three-level *LLC* converters and eight HBs) was built to verify the effectiveness and feasibility of the proposed control method, shown in Fig. 13. The control system is composed of a TMS320F28374 processor for master controller and two TMS320F280049 processors functioned as HB controller and *LLC* controller for each module. A Chroma 62150H-1000S PV simulator is connected to common dc bus to power the whole system, and a Chroma 61860 grid simulator is used to simulate three-phase ac grid, whose output voltage is 120 V/50 Hz. The reference value of HB dc-bus voltage is set to 17.5 V, so the modulation index $\mathrm{S_T}$ of the experiment prototype is $120/(17.5\times 8) = 0.8571$, which is slightly lower than 0.8696, so the previous analysis of active power backflow zone in Fig. 11 is applicable. The rated power of the experimental prototype is 3600 W, so the rated grid current amplitude is 20 A. Other principal parameters of the prototype are given in Table IV. Although the power and voltage levels of the experimental prototype in our laboratory are relatively low, its topology structure is completely consistent with that in Fig. 1, and it is competent to verify the proposed control strategy.

The first experiment starts with the condition that the output power is 720 W ($\mathrm{R_P} = 720/3600 = 0.2$). At a certain time, interphase short-circuit fault between phases B and C occurs,

TABLE III
CORE IDEA OF DIFFERENT CONTROL METHODS AND THE AREA COMPARISON OF ACTIVE POWER BACKFLOW ZONE

Control Strategy	Core Ideas	The Area of active power backflow zone	Reduced Area Compared to the ACIS, $(S_1\text{-}S_i)/S_1\times100\%$, i=1,2,3,4,5
ACIS	Inject positive-sequence active current based on (29)	0.11912	0%
ZSVCS	Compensate fundamental-frequency zero-sequence voltage based on (7)	0.11928	-0.067%
AZSVCS	Compensate adaptive fundamental-frequency zero-sequence voltage based on (36) and (37)	0.04288	64%
MSHZSVCS	Compensate fundamental-frequency and multiple specific harmonic zero-sequence voltages	0.00699	94.13%
Combined Control Method of AZSVCS and MSHZSVCS	Compensate adaptive fundamental-frequency and multiple specific harmonic zero-sequence voltages	0.00174	98.54%

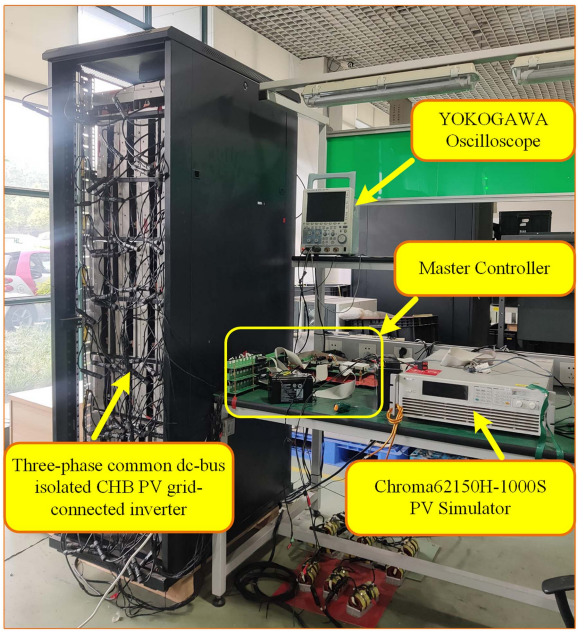

Fig. 13. Experimental prototype of the three-phase common DC-bus isolated CHB PV grid-connected inverter.

TABLE IV
EXPERIMENTAL PARAMETERS

Symbol	PARAMETER	Value
U_{ref}	HB dc-bus voltage reference	17.5 V
L_f	Grid side filter inductance	1.5 mH
f_{HB}	HB switching frequency	2000 Hz
C_{Xij}	HB dc-bus capacitance	18.8 mF(4700 μF×4)
L_{rXi}	Resonant inductance	180 μH
C_{rXi}	Resonant capacitance	56 nF
L_{mXi}	Magnetizing inductance	2 mH
N_T	Turn ratio of LLC transformer	21
f_{LLC}	Rated switching frequency of LLC	50000 Hz

and drop depth is zero ($D = 0$, line-voltage $u_{gBC} = 0$, $u_{gB} = u_{gC} = -0.5u_{gA}$), shown in Fig. 14(a). According to (2) and (6), reactive current reference I^*_{qP} is 8A and active current reference I^*_{dP} are calculated as 8A during LVRT. From to the analysis of [15], only when I^*_{dP} is greater than 13.856 A in this scenario can active power backflow be suppressed. Therefore, active power backflow will occur in phase B. The experimental waveforms of i_{gA} and U_{HB11} are shown in Fig. 14(b), where

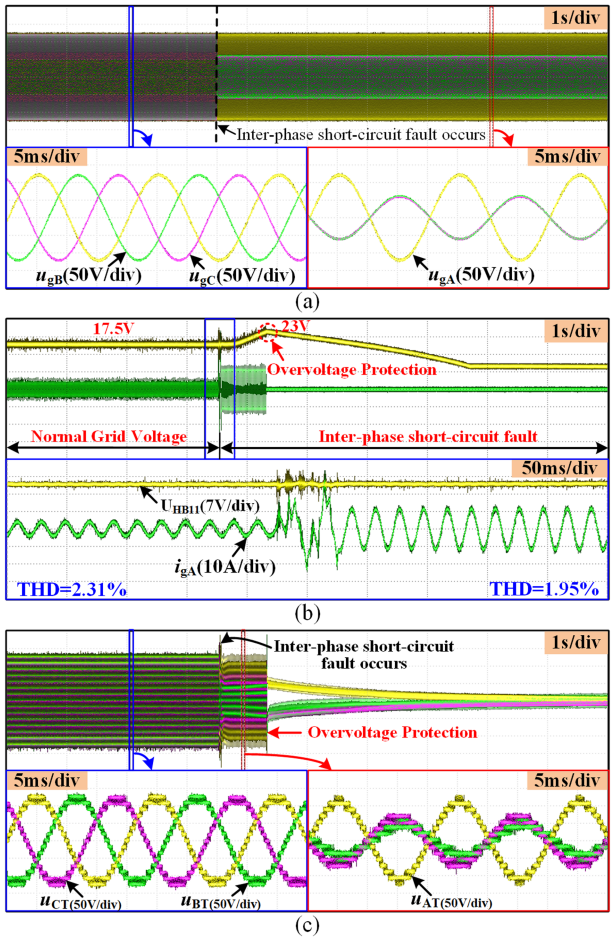

Fig. 14. Output waveforms of the first experiment. (a) u_{gA}, u_{gB}, and u_{gC} before and after grid voltages sag. (b) i_{gA} and U_{HB11}. (c) u_{AT}, u_{BT}, and u_{CT}.

U_{HB11} continues to increase rapidly from 17.5 to 23 V after interphase short-circuit occurs, resulting in that the overvoltage protection is triggered and the inverter is shut down. In addition, the ac output voltages of CHB inverter, u_{AT}, u_{BT}, and u_{CT} are shown in Fig. 14(c), which are standard multi-level step waveforms before grid voltage sag.

The second experiment starts with the condition same as the first experiment, but the AZSVCS in [22] is adopted. In this scenario, after interphase short-circuit fault occurs, reactive current and active current reference are calculated as 8 and 8 A, respectively, so the adaptive compensation coefficient must

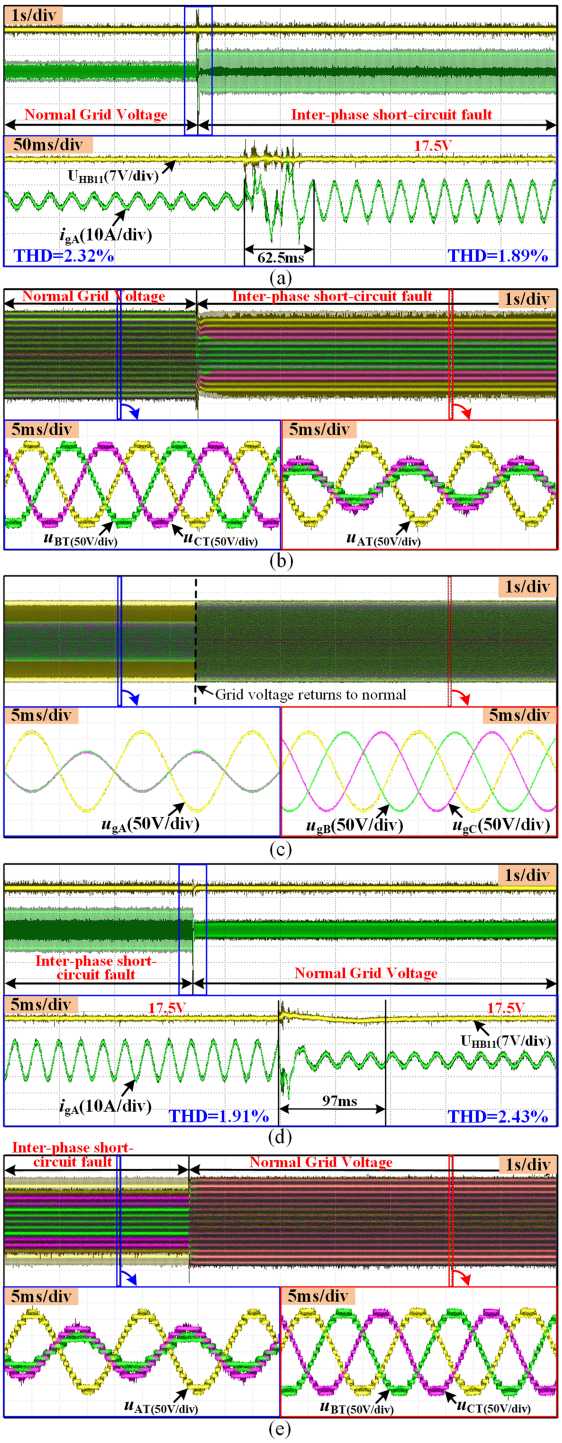

Fig. 15. Output waveforms of the second experiment. (a) Transient process of i_{gA} and U_{HB11} when grid voltages sag. (b) u_{AT}, u_{BT}, and u_{CT} when grid voltages sag. (c) u_{gA}, u_{gB}, and u_{gC} before and after grid voltages recover. (d) Transient process of i_{gA} and U_{HB11} when grid voltages recover. (e) u_{AT}, u_{BT}, and u_{CT} when grid voltages recover.

be greater than 0.268 based on (37), which is set to 0.3 in this experiment to retain a certain margin. Based on Fig. 11(f), when $R_P = 0.2$ and $D = 0$, the CHB inverter will operate outside the active power backflow zone for this method, so the active power backflow can be avoided, and the experimental results

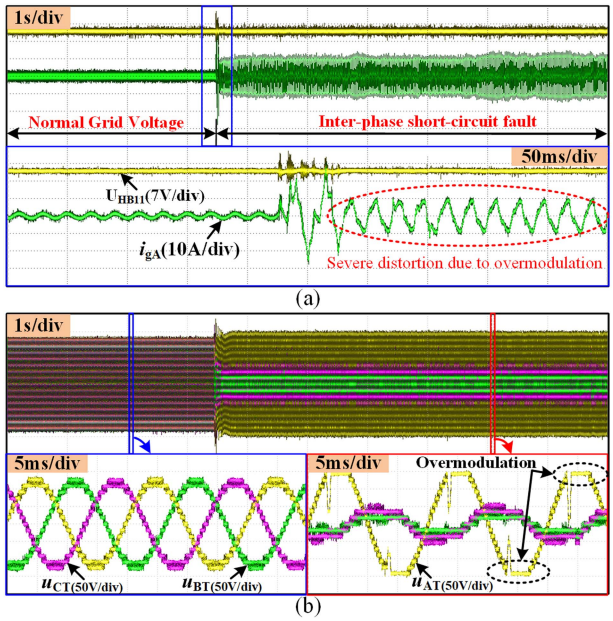

Fig. 16. Output waveforms of the third experiment. (a) i_{gA} and U_{HB11} when grid voltages sag. (b) u_{AT}, u_{BT}, and u_{CT} when grid voltages sag.

are given in Fig. 15. When the grid voltages of phases B and C sag, the experimental waveforms are given in Fig. 15(a) and (b). When the grid voltages of phases B and C recover, the experimental waveforms are shown in Fig. 15(c)–(e). As could be seen, U_{HB11} is capable of being maintained at 17.5 V, which means that active power backflow is effectively suppressed. In addition, the dynamic response time of grid current is 62.5 and 97 ms, respectively, in case of grid voltages sag and recovery, meeting LVRT requirement.

The third experiment begins with the condition that the output power of PV simulator is 240W ($R_P = 240/3600 = 0.067$), and the line voltage u_{BC} drops to zero ($D = 0$) at a certain time, shown in Fig. 14(a). According to Fig. 11(f), with R_P reduced from 0.2 to 0.067, if AZSVCS is adopted, the inverter will be overmodulation, and the experimental results are shown in Fig. 16. As could be seen, when the grid voltages drop, the CHB inverter operates unstable and the grid current is seriously distorted due to overmodulation, which does not meet the requirements of grid-tied standards.

The fourth experiment is dedicated to evaluating the performance of the combination control method of AZSVCS and MSHZSVCS, which has the same experiment conditions as the third. In this scenario, after interphase short-circuit fault occurs, reactive current and active current reference are calculated as 2.67 and 8 A, respectively, so the adaptive compensation coefficient must be greater than 0.6769 based on (37), which is set to 0.7 in this experiment. According to the analysis of Fig. 11(f), when $R_P = 0.067$ and $D = 0$, the system operates outside the active power backflow zone for this method, so the active power backflow problem can be avoided, and the experimental results are shown in Fig. 17. When the grid voltages of phases B and C sag, the experimental waveforms are given in Fig. 17(a)–(c). When the grid voltages of phases

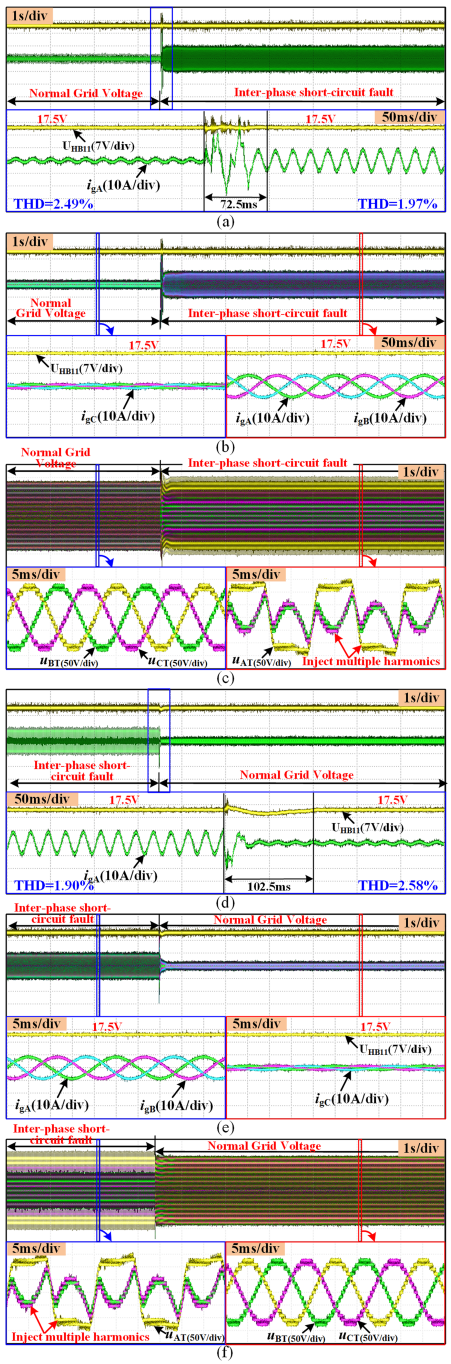

Fig. 17. Output waveforms of the fourth experiment. (a) Transient process of i_{gA} and U_{HB11} when grid voltages sag. (b) Steady-state waveforms of i_{gA}, i_{gB}, and i_{gC} before and after grid voltages sag. (c) u_{AT}, u_{BT}, and u_{CT} before and after grid voltages sag. (d) Transient process of i_{gA} and U_{HB11} when grid voltages recover. (e) Steady-state waveforms of i_{gA}, i_{gB}, and i_{gC} before and after grid voltages recover. (f) u_{AT}, u_{BT}, and u_{CT} before and after grid voltages recover.

B and C recover, the experimental waveforms are shown in Fig. 17(d)–(f). As could be seen, U_{HB11} is capable of being maintained at 17.5 V, which means that active power backflow is effectively suppressed. From Fig. 17(b) and (e), the waveform of three-phase grid current is a standard sine waveform before grid voltages sag, so there is no overmodulation, which conforms to theoretical analysis. In addition, the dynamic response time of grid current is 72.5 ms in case of voltage drop and 102.5 ms in case of grid voltage recovery. As can be seen from Fig. 17(c) and (f), the output voltages on the ac side of CHB inverter are no longer a standard multi-level waveform, which is due to the use of the proposed control strategy to inject multiple specific harmonic zero-sequence voltages for lowering the modulation voltage amplitude.

VI. Conclusion

In this article, the control strategies for suppressing active power backflow of three-phase common dc-bus isolated CHB PV grid-connected inverters under interphase short-circuit conditions are proposed, which are all capable of significantly shrinking active power backflow zone compared with the existing methods and improving the adaptability of the inverter to different output power and different drop depths during LVRT. The main conclusions are as follows.

1) Compared with the existing control strategies, the proposed MSHZSVCS has the smallest active power backflow zone, that is, the strongest ability to suppress active power backflow.
2) Considering the control performance and computational complexity, the proposed MSHZSVCS in this article only compensates the third, fifth, seventh and ninth harmonics. To further reduce the area of active power backflow zone, the number of compensated harmonic can continue to increase.
3) The combination control method of AZSVCS and MSHZSVCS is recommended in practical application, which has the optimal performance and will reduce the area of active power backflow zone by 98.54% compared to the ACIS.

Appendix

For the AZSVCS, the original curve W_{III} and the fitting curve $W_{\mathrm{III}}*$ is shown in Fig. 18, where their residual is less than 0.3%. Therefore, curve $W_{\mathrm{III}}*$ with known expression can be used to replace W_{III} when calculating the area of active power backflow zone.

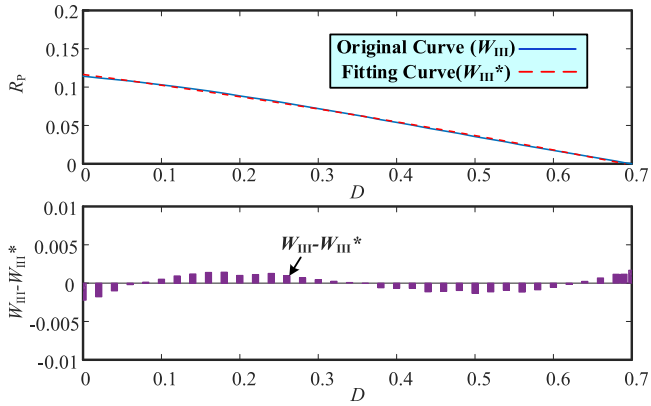

Fig. 18. Two-order curve fitting of W_{III} and residual.

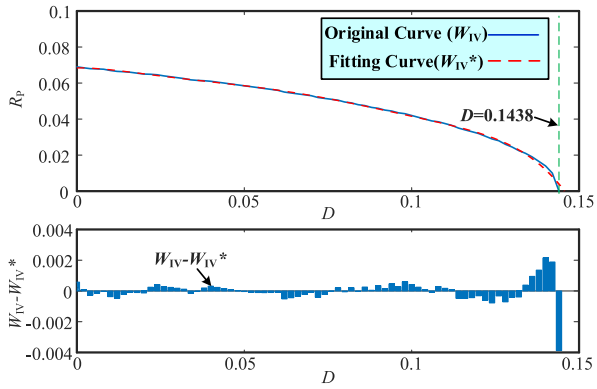

Fig. 19. Six-order curve fitting of W_{IV} and residual.

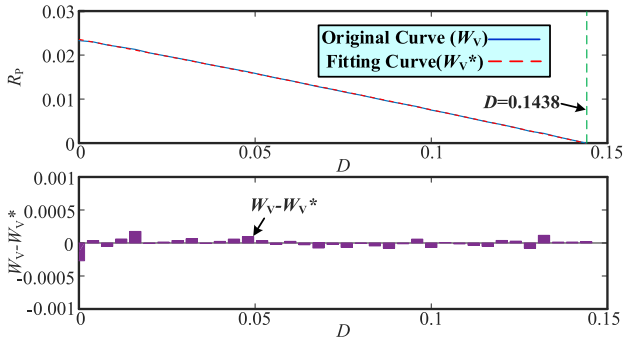

Fig. 20. Two-order curve fitting of W_V and residual.

For the proposed MSHZSVCS, the original curve W_{IV} and the fitting curve $W_{IV}*$ is shown in Fig. 19, where their residual is less than 0.4%. Therefore, curve $W_{IV}*$ is able to be adopted to replace W_{IV} when calculating the area of active power backflow zone.

For the combination control method of AZSVCS and MSHZSVCS, the original curve W_V and the fitting curve W_V* is shown in Fig. 20, where their residual is less than 0.3%. Therefore, curve W_V* is able to be adopted to replace W_V when calculating the area of active power backflow zone.

REFERENCES

[1] REN21, "Renewables 2022 global status report.REN21," 2022 [Online]. Available: https://www.ren21.net/gsr-2022/chapters/chapter_01/chapter_01/

[2] H. Choi, M. Ciobotaru, and V. G. Agelidis, "Cascaded H-bridge converter with multi-phase isolated DC/DC converter for large-scale PV system," in *Proc. IEEE Int. Conf. Ind. Technol.*, 2014, pp. 455–461.

[3] F. Zhang et al., "Design and demonstration of a SiC-based 800V/10kV 1MW solid-state transformer for grid-connected photovoltaic systems," in *Proc. IEEE 3rd Int. Future Energy Electron. Conf. Energy Convers. Congr. Expo. Asia*, 2017, pp. 1987–1990.

[4] T. Liu et al., "High-efficiency control strategy for 10-kV/1-MW solid-state transformer in PV application," *IEEE Trans. Power Electron.*, vol. 35, no. 11, pp. 11770–11782, Nov. 2020.

[5] N. A. Awadhi and M. S. E. Moursi, "A novel centralized PV power plant controller for reducing the voltage unbalance factor at transmission level interconnection," *IEEE Trans. Energy Convers.*, vol. 32, no. 1, pp. 233–243, Mar. 2017.

[6] F. V. Amaral, T. M. Parreiras, G. C. Lobato, A. A. P. Machado, I. A. Pires, and B. de Jesus Cardoso Filho, "Operation of a grid-tied cascaded multilevel converter based on a forward solid-state transformer under unbalanced PV power generation," *IEEE Trans. Ind. Appl.*, vol. 54, no. 5, pp. 5493–5503, Sep./Oct. 2018.

[7] Y. Yu, G. Konstantinou, B. Hredzak, and V. G. Agelidis, "On extending the energy balancing limit of multilevel cascaded H-bridge converters for large-scale photovoltaic farms," in *Proc. Australas. Universities Power Eng. Conf.*, 2013, pp. 1–6.

[8] L. Wang, D. Zhang, Y. Wang, B. Wu, and H. S. Athab, "Power and voltage balance control of a novel three-phase solid-state transformer using multilevel cascaded H-bridge inverters for microgrid applications," *IEEE Trans. Power Electron.*, vol. 31, no. 4, pp. 3289–3301, Apr. 2016.

[9] Y. Yu, G. Konstantinou, B. Hredzak, and V. G. Agelidis, "Power balance optimization of cascaded H-bridge multilevel converters for large-scale photovoltaic integration," *IEEE Trans. Power Electron.*, vol. 31, no. 2, pp. 1108–1120, Feb. 2016.

[10] S. Rivera, B. Wu, S. Kouro, H. Wang, and D. Zhang, "Cascaded H-bridge multilevel converter topology and three-phase balance control for large scale photovoltaic systems," in *Proc. 3rd IEEE Int. Symp. Power Electron. Distrib. Gener. Syst.*, 2012, pp. 690–697.

[11] T. Liu et al., "Design and implementation of high efficiency control scheme of dual active bridge based 10kV/1MW solid state transformer for PV application," *IEEE Trans. Power Electron.*, vol. 34, no. 5, pp. 4223–4238, May 2019.

[12] W. Mao et al., "Research on power equalization of three-phase cascaded H-bridge photovoltaic inverter based on the combination of hybrid modulation strategy and zero-sequence injection methods," *IEEE Trans. Ind. Electron.*, vol. 67, no. 11, pp. 9337–9347, Nov. 2020.

[13] Y. Yu, G. Konstantinou, C. D. Townsend, and V. G. Agelidis, "Comparison of zero-sequence injection methods in cascaded H-bridge multilevel converters for large-scale photovoltaic integration," *Inst. Eng. Technol. Renew. Power Gener.*, vol. 11, no. 5, pp. 603–613, 2017.

[14] X. Zhang, T. Zhao, W. Mao, D. Tan, and L. Chang, "Multilevel inverter for grid-connected photovoltaic applications: Examining emerging trends," *IEEE Power Electron. Mag.*, vol. 5, no. 4, pp. 32–41, Dec. 2018.

[15] T. Zhao and D. Chen, "Analysis and suppression of active power backflow of three-phase common dc-bus cascaded H-bridge PV grid-connected inverter during LVRT," *IEEE J. Emerg. Sel. Topics Power Electron.*, vol. 10, no. 1, pp. 745–759, Feb. 2022.

[16] X. He, H. Geng, R. Li, and B. C. Pal, "Transient stability analysis and enhancement of renewable energy conversion system during LVRT," *IEEE Trans. Sustain. Energy*, vol. 11, no. 3, pp. 1612–1623, Jul. 2020.

[17] H. D. Tafti, A. I. Maswood, G. Konstantinou, C. D. Townsend, P. Acuna, and J. Pou, "Flexible control of photovoltaic grid-connected cascaded H-bridge converters during unbalanced voltage sags," *IEEE Trans. Ind. Electron.*, vol. 65, no. 8, pp. 6229–6238, Aug. 2018.

[18] A. kumar, A. Narula, and V. Verma, "Low voltage ride through (LVRT) strategies for single phase grid connected PV fed cascaded multilevel inverter," in *Proc. IEEE Int. Conf. Power Electron., Drives Energy Syst.*, 2020, pp. 1–6.

[19] R. Sharma and A. Das, "Analysis of solar PV fed cascaded H-bridge converter during low voltage ride operation," in *Proc. IEEE Int. Conf. Power Electron., Drives Energy Syst.*, 2020, pp. 1–6.

[20] H. Li, Z. Gao, S. Ji, Y. Ma, and F. Wang, "An inrush current limit method for SiC-based multi-level grid-connected converter during low voltage ride through," in *Proc. IEEE Appl. Power Electron. Conf. Expo.*, 2021, pp. 2044–2049.

[21] T. Zhao and D. Chen, "Active power backflow control strategy for cascaded photovoltaic solid-state transformer during low voltage ride through," *IEEE Trans. Ind. Electron.*, vol. 69, no. 1, pp. 440–451, Jan. 2022.

[22] T. Zhao, Z. Feng, M. Wang, M. Wu, and D. Chen, "An optimized LVRT control strategy of cascaded modular medium-voltage inverter for large-scale PV power plant," *IEEE J. Emerg. Sel. Topics Power Electron.*, vol. 10, no. 6, pp. 7744–7759, Dec. 2022.

[23] Y. Ko, M. Andresen, K. Wang, and M. Liserre, "Modulation for cascaded multilevel converters in PV applications with high input power imbalance," *IEEE Trans. Power Electron.*, vol. 36, no. 9, pp. 10866–10878, Sep. 2021.

[24] P. Rodriguez, J. Pou, J. Bergas, J. I. Candela, R. P. Burgos, and D. Boroyevich, "Decoupled double synchronous reference frame PLL for power converters control," *IEEE Trans. Power Electron.*, vol. 22, no. 2, pp. 584–592, Mar. 2007.

[25] T. Zhao et al., "Analysis and suppression of resonant current envelope ripple of LLC converter in cascaded modular PV solid-state transformer," *IEEE J. Emerg. Sel. Topics Power Electron.*, vol. 9, no. 3, pp. 3744–3757, Jun. 2021.

Tao Zhao was born in Henan, China, in 1991. He received the B.S. degree in electrical engineering and automation from Xi'an Technological University, Xi'an, China, the M.S. degree in power electronics and power drives and the Ph.D. degree in electrical engineering from Hefei University of Technology, Hefei, China, in 2014, 2017, and 2020, respectively.

Since 2020, he has been with the Faculty of College of Electrical Engineering, Qingdao University, Qingdao, China. His current research interests include the modeling and control of power converters, and multilevel converters.

Zixiang Sun (Student Member, IEEE) was born in Anhui, China, in 1999. He received the B.S degree in electrical engineering and automation from Anhui Polytechnic University, Wuhu, China, in 2022. He is currently working toward the M.S. degree in electrical engineering with the School of Electrical Engineering, Qingdao University, Qingdao, China.

His current research interests include the modeling and control of power converters, and multilevel converters.

Zhijian Feng was born in Shandong, China, in 1992. She received the B.S. and Ph.D. degrees in electrical engineering from Hefei University of Technology, Hefei, China, in 2014 and 2020, respectively.

She is currently a Lecturer with the College of Electrical Engineering, Qingdao University, Qingdao, China. Her current research interests include application of SiC devices, loss analysis and thermal modeling and power electronics conversion.

Mingda Wang (Student Member, IEEE) was born in Anhui, China, in 1996. He received the B.S degree in electrical engineering and automation in 2017 from Hefei University of Technology, Hefei, China, where he is currently working toward the Ph.D. degree in electric engineering with the School of Electrical Engineering and Automation.

His current research interests include the control of power converters, and photovoltaic generation technologies.

Mengze Wu (Student Member, IEEE) was born in Anhui, China, in 1998. She received the B.S degree in electrical engineering and automation in 2020 from Hefei University of Technology, Hefei, China, where she is currently working toward the Ph.D. degree in electric engineering with the School of Electrical Engineering and Automation.

Her current research interests include the modeling and control of power converters, and photovoltaic generation technologies.

Xing Zhang (Senior Member, IEEE) was born in Shanghai, China, in 1963. He received the B.S., M.S. and Ph.D. degrees in electric engineering and automation from Hefei University of Technology, Hefei, China, in1984, 1990, and 2003, respectively.

Since 1984, he has been a Faculty Member with the School of Electric Engineering and Automation, Hefei University of Technology, where he is currently a Professor and also serves as the Chief of National and Local Joint Engineering Laboratory for Renewable Energy Access to Grid Technology. He is also with the Photovoltaic Engineering Research Center of Ministry of Education. His main research interests include photovoltaic generation technologies, wind power generation technologies, and distributed generation system.